# A Multi-cavity Touch Interface for a Flexible Soft Laparoscopy Device: Design and Evaluation

Jialei Shi, *Student Member, IEEE,* Ge Shi, *Member, IEEE*, Yu Wu, *Member, IEEE*, and Helge A. Wurdemann, *Member, IEEE*

*Abstract*—edical instruments made of compliant materials provide increased safety and dexterity when interacting with anatomical environments.edical instruments made of compliant materials provide increased safety and dexterity when interacting with anatomical environments.M Beyond the development of hardware, the maneuverability of these medical instruments presents significant challenges, especially in practical applications like minimally invasive surgery. Consequently, developing efficient and intuitive interfaces for operating these soft instruments is crucial. This study focuses on creating a flexible, soft robotic handheld laparoscopy device featuring a multi-cavity touch interface. The pneumatically driven soft robotic device has a continuum structure and an outermost diameter of 11.5 mm. The laparoscopy device is equipped with a silicone-cast touch interface that includes five air-filled cavities. Monitoring the pressure within these cavities facilitates the identification of user inputs, offering an intuitive and cost-effective way to operate the device. To evaluate the laparoscopy device's performance, *in vitro* tests were conducted using a test rig and a phantom environment. The device's usability was assessed by participants, providing valuable insights into its functionality and practicality in a controlled setting. These evaluations lay the groundwork for future advancements in soft robotic medical instruments for minimally invasive procedures.

*Index Terms*—Pneumatic-driven soft robots, laparoscopy device, touch interface, soft medical devices.

## I. INTRODUCTION

**T**HE medical sector has placed significant emphasis on enhancing the controllability and automation levels of medical devices to achieve safe and efficient robot-assisted surgeries [1]. In this context, the intuitive and cost-effective operation of medical robots becomes imperative. Tele-operation, exemplified by platforms like the da Vinci surgery system, offers precise and stable control. In addition, Instruments made of compliant materials are particularly advantageous

Jialei Shi, Ge Shi and Helge A. Wurdemann are with the Department of Mechanical Engineering, University College London, London, UK. (e-mail: h.wurdemann@ucl.ac.uk).

Jialei Shi is also with the Mechatronics in Medicine, The Hamlyn Centre for Robotic Surgery, Department of Mechanical Engineering, Imperial College London, UK. (e-mail: j.shi@imperial.ac.uk).

Ge Shi is also with the Robotics and Autonomous Systems, Data61, Commonwealth Scientific and Industrial Research Organisation, Brisbane, Australia (ge.shi@deta61.csiro.au).

Yu Wu is with the Department of Electronic and Electrical Engineering, University College London, London, UK. (e-mail: yu.wu.09@ucl.ac.uk).
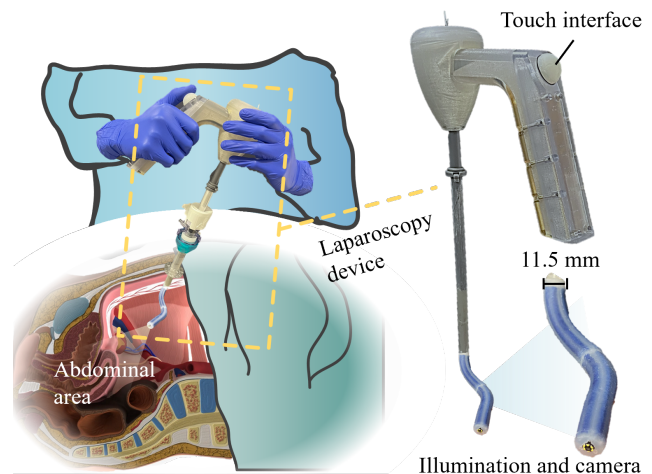


Fig. 1. Illustration of the handheld flexible soft robotic laparoscopy device during the operation.

when interacting with environments and navigating in tortuous anatomical environments with constrained spaces [2]–[4]. As such, the utilisation of soft and compliant robots has played a crucial role in developing tools that are inherently safe and dexterous for a range of medical and healthcare applications, examples including minimally invasive surgery (MIS) [5]–[8], rehabilitation and assistance [9]–[11], and variable haptic devices [12]–[14].

A wide spectrum of soft robotic devices, either fully or partially made of compliant structures, have been devised for various MIS applications, such as brain [15], lung [16], [17], heart [18], [19] and vasculature [20], [21] interventions, collectively improving surgical outcomes and patient care. In the field of endoluminal intervention, MIS might involve the introduction of medical tools into the insufflated abdomen through small incisions (e.g., between 5-12 mm in diameter) to perform surgical tasks, assisted by a rigid laparoendoscope with vision devices. Soft robots have been extensively explored to augment the dexterity of laparoendoscopes [22]. Noteworthy examples include a low-cost disposable continuum endoscope [23], featuring a flexible extruded catheter and a parallel bellow soft actuator at the tip. Similarly, the HydroJet device [24], designed for upper gastrointestinal tract cancer screening, employs a capsule with four fluid exhaust ports connected to the tip of a soft catheter. Actuation of the catheter is achieved by expelling pressurised water from the capsule. Addressing challenges in colorectal surgery, pneumatic-driven soft robots have been devised [25]–[27]. For instance, a highly

dexterous two-segment soft instrument was proposed in [28], where the robot was pneumatically driven and featured six reinforced actuation chambers. These advancements in soft medical devices underscore their potential and versatility in various healthcare applications. In addition, the development of highly effective yet cost-efficient operation systems for medical robots, in combination with soft robotic devices, has the potential to substantially reduce operation time, enhance surgeons' dexterity, and improve the accessibility of soft medical instruments.

Considerable efforts have been dedicated to achieving intuitive and effective operations of these soft and compliant robots [29]. In this context, users typically control these robots through either physical or virtual input interfaces. While virtual interfaces offer a cost-effective solution, they often lack the sense of touch [30], [31]. Commercially available products, such as the Geomagic Touch [32]–[34] or joystick [35], can serve as input devices, with the potential to restore touch or contact feedback from these devices [36]. Researchers have also developed alternative interfaces, such as the 3D haptic trackball interface in [37]. A more intuitive approach involves considering the unique structures of soft robots when designing input devices. For instance, input devices may share similar continuum structures with soft robots. In controlling the bellow-type robot reported in [23], a snake-like, continuum user interface with multiple backbones was proposed in [38]. This manual interface varied syringe pistons directly to control the pressure in bellows. Likewise, continuum interfaces were introduced in [39], [40] for controlling continuum robots. To simplify the structure complexity of continuum interfaces, [41] presented a 3D printed interface with a flexible mesh structure for soft growing robots. An inertial measurement unit attached at the interface's tip estimated its pose, and the desired control signal was calculated based on this pose information. The study in [42] investigated a variable-stiffness interface with a rod structure, and the stiffness was adjusted via the fibre jamming technique. Additionally, the body motions of users were captured and utilised to control soft robots, as illustrated in [43]. However, it is important to note that motion tracking systems are often associated with high costs. Notably, works in [38], [44] present approaches that eliminate the need for electronic devices to generate pressure, instead relying on mechanically controlling the positions of syringe pistons to generate pressure.

In summary, the aforementioned works have typically approached the design of soft robots and control interfaces as separate entities. For MIS applications, research demonstrates that handheld devices can enhance both ergonomics and dexterity, offering potential improvements in the quality of various surgical procedures [45], [46], such as transurethral surgery [47], laparoscopic surgery [48], and orthopedic surgery [49]. The control interfaces of these handheld devices often include handle control (e.g., via the user's wrist/hand), thumb control, and mixed control methods. Moreover, it has been observed that finger-operated interfaces are more ergonomic than wrist controls, while providing comparable surgical performance [50]. As such, a compact handheld soft robotic medical device that integrates both soft robots and
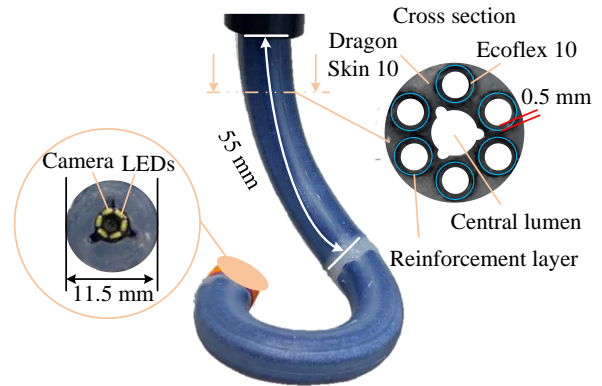


Fig. 2. Two-segment soft robotic instrument with an integrated tip camera. Detailed cross-sectional dimensions are reported in [51].

control interfaces should benefit the medical sector. However, this concept seems to be underexplored.

The contribution of this work lies in the design and characterisation of a handheld flexible soft robotic laparoscopy device featuring an integrated multi-cavity touch interface, as illustrated in Fig. 1. The soft robot is directly controlled via the touch interface. This pneumatically driven soft robot has a continuum structure with a diameter of 11.5 mm. The touch interface, made of silicone, comprises five air-filled cavities. The variations in cavity pressure within the touch interface are mapped to the motion of the soft robot, with the sensitivity of the touch interface adjustable by gain factors. Experiments were conducted to validate the corresponding control strategy and to evaluate the usability of the flexible soft robotic laparoscopy device in a phantom environment.

The rest of this paper is organised as follows: Section II details the hardware design and system integration of the developed soft robotic laparoscopy device. The characterisation of the soft robot and the touch interface is then reported in Section III. Section IV outlines the forward kinematics model for real-time robot visualisation and elaborates on the control strategy mapping user input to robot motions. Section V demonstrates the experimental evaluation of the design system and the validation of the control strategy. The corresponding discussions of the designed system and experiment evaluation are presented in Section VI. Section VII concludes this work.

## II. HARDWARE DESIGN AND SYSTEM INTEGRATION

### A. Design of the Soft Robot

The soft robot developed in this work is pneumatically-driven and features reinforced circular chambers. The fundamental design and the manufacturing process of the soft robot are based on the STIFF-FLOP manipulator [52], devised for minimally invasive surgery. This robot features fully reinforced circular actuation chambers that allow elongation while constraining radial inflation. In this way, the pressurisation does not change the shape and perimeter of all actuation chambers, ensuring that the actuated chambers do not squeeze the central working channel and the cables passing through it. To achieve bending motion in all directions (i.e., $0 \sim 360°$)
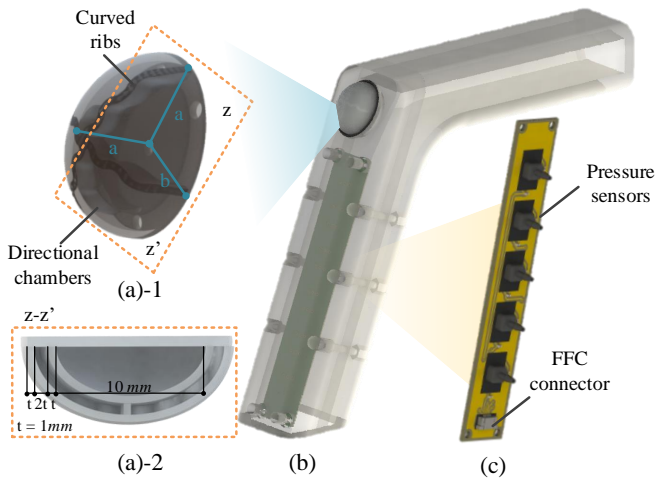
Fig. 3. Design of the touch interface: (a)-1 Top view of the multi-cavity touch interface sized in $a = 6$ mm, $b = 5$ mm. (a)-2 Double-layer structure of the touch interface (thickness of layers is $1$ mm). (b) Schematic illustration of the multi-cavity touch interface mounted to a handle. (c) Self-developed PCB for pressure sensing.

with lower required actuation pressure, two adjacent chambers are internally connected and actuated as one pair.

Each actuation chamber has a diameter of 1.5 mm. The outermost diameter of the soft robot is 11.5 mm, designed to fit the commercially available 12 mm trocar [22]. To accommodate an endoscope camera with a 4 mm diameter [OV9734, China], an inner lumen of 4.5 mm diameter is preserved. The entire length of one robot segment is 59 mm. Fig. 2 illustrates the soft robot with an integrated camera, capable of achieving omni-directional bending and elongation motions. Details of a multiple-step fabrication process and cross-sectional dimensions of this robot are reported in [31] and [51], respectively. It is important to note that Ecoflex 50 [Smooth-On, US] is typically used to fabricate the large-scale STIFF-FLOP manipulators (e.g., with a diameter of 25 mm). [52]. However, in this work, the robot's body is constructed from Dragon Skin 10 [Smooth-On, US] to enhance its stiffness as the robot's diameter is reduced. Moreover, Ecoflex 10 [Smooth-On, US] is used for fabricating the 1.5 mm inner chamber to facilitate the fabrication. Specifically, in the step of creating the 1.5 mm chambers, silicone needs to be injected with a syringe due to the narrow space constraints. Ecoflex 10, having lower viscosity compared to Dragon Skin 10, is easier to inject.

### B. Design of the Multi-cavity Touch Interface

Fig. 3 illustrates the design of the touch interface for flexible laparoscopy, featuring a double-layer soft structure with five cavities in total. The pressure in each cavity is monitored by five pressure sensors [Honeywell ABPDANT005PGAA5, US]. The pressure measurement range of the sensor is 0∼34.5 KPa.

The soft structure, designed to sense touch information from users, adopts an ellipsoid shape, measuring $a = 6$ mm and $b = 5$ mm. This size aligns with the average adult thumb, as noted by [53]. The soft structure incorporates five cavities across two layers: four quadrant-shaped cavities in the first

layer, separated by curved ribs, and a single cavity in the second layer [54]. In the cross-sectional view presented in Fig. 3, the elastic membranes are $1$ mm thick, while the curved ribs, forming the cavities, have a height of $2$ mm. The dimensions of the inner ellipsoid cavity are $a = 5$ mm and $b = 4$ mm. Curved ribs are designed to minimise compression strength and mitigate the buckling effect. They also serve to partition the first-layer cavities and to provide different pressure responses. The double-layer design mitigates the buckling of the curved ribs, reducing pressure interferences between the directional chambers. Additionally, the soft button is designed for direct user interaction, considering the touch intuitiveness and user acceptance. The four directional cavities are similar to commonly used joysticks, such as those on Xbox devices, where buttons are typically arranged in a quadrant. This familiar arrangement is likely to enhance user control and comfort.

The soft structure is composed of Dragon Skin 20 [Smooth-On, US]. In the cavities of the soft structure, air functions as the medium to transmit the touch signal to the pressure sensor in the form of pressure variations. Fig. 3 also reports five pressure sensors soldered onto a designed Printed Circuit Board (PCB), which monitors pressure changes in the five cavities during use. This PCB is mounted on the handle, and the pressure information is utilised to control motions of the soft robot. By touching different cavities in the first layer, the soft robot is actuated to achieve corresponding bending movements. Once the centre chamber formed by the second layer is stimulated, the soft robot will achieve elongation motions. The control strategy is further elaborated in Section IV-B.

### C. System Integration

Fig. 4 illustrates the integrated system of the soft robotic laparoscopic device. Fig. 4(a) shows that the entire medical device comprises the handle assembly, the touch interface, the flexible soft robot with an integrated camera, a sliding sleeve, and a micro-controller (i.e., Arduino DUE). The micro-controller is capable of monitoring the pressure variation in the touch interface and controlling the chamber pressure of the soft robot. Six proportional pressure regulators [Camozzi K8P, Italy] are used to adjust the chamber pressure of the soft robot. Furthermore, a host computer communicates with the micro-controller and the camera, facilitating data recording and image visualisation. Python script adjusts the camera view to align with the motion of the robot. Please note that the nominal actuation pressure of the soft robot ranges from 0 to 1.8 bar. In most operating rooms, pressurised air systems (exceeding 7 bar) are commonly used to power ventilators and surgical tools, such as drills. For instance, some surgical tools require an operating pressure of 7 bar, which is significantly higher than the pressure needed for our device. If a hospital does not have a compressed air system, portable air compressors are readily available on the market.

During the operation, trocar seals prevent air from escaping the abdomen and maintain internal air pressure to provide surgeons with a clear operating area. However, trocar seals
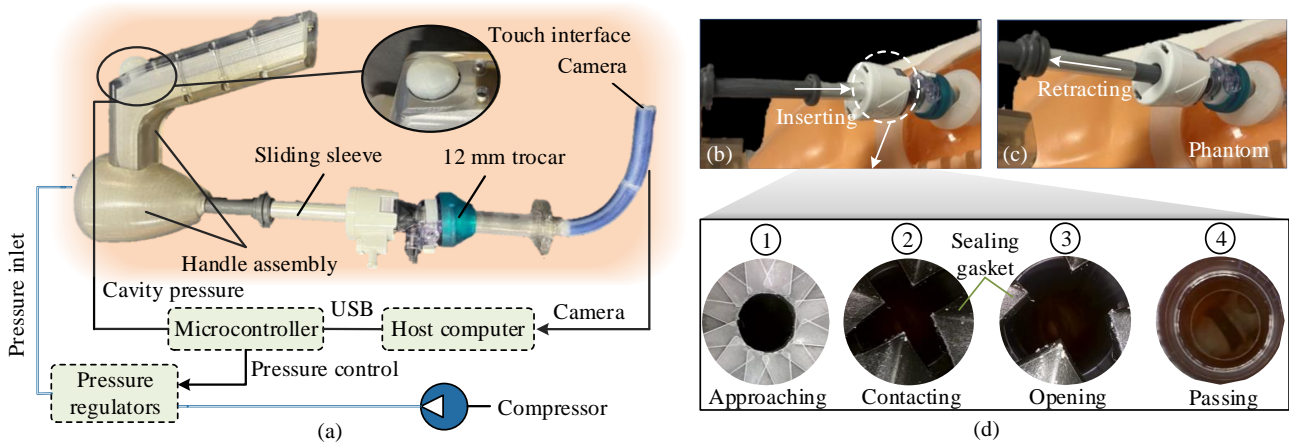
Fig. 4. (a) Assembly of the handheld soft robotic laparoscopy device with a multi-cavity touch interface. Operating the device in a phantom environment, when (b) inserting and (c) retracting the sliding sleeve. (d) The camera view when inserting the soft robotic device to a 12 mm trocar port.

introduce friction, which can lead to a buckling effect in the soft robot. To address this issue, the sliding sleeve can open the sealing gasket of the trocar during the insertion of the soft robot (see Fig. 4(b)). Once the soft robot passes through the trocar port, the sliding sleeve is retracted, allowing the trocar seals to function normally during the operation. Fig. 4(d) shows the camera view capturing the insertion of the soft robot into the abdominal area of a phantom via the trocar port. In stage 1, the trocar seals are fully closed. As the sliding sleeve pushes through the sealing gaskets, the trocar seal transitions from stage 2 to stage 3, opening up. The soft, flexible robotic tip can then pass through the trocar seals directly, as illustrated in stage 4.

## III. CHARACTERISATION OF THE SOFT ROBOT AND THE TOUCH INTERFACE

### A. Characterisation of the Soft Robot

Typically, miniaturised lightweight endoscope cameras weigh only a few grams, for instance, 2.6 g [RA78080A-60 Bangu Technology] as reported in [23], and approximately 1.0 g (OV 7934) in our specific application. Additionally, studies have found that interaction forces between instruments and organs vary widely, ranging from 0.1 to 10 N during traditional laparoscopy procedures [55]. These forces are impacted by factors such as the type of gesture performed and the operator's experience. In this study, our objective is to apply the soft robot with a tip-mounted camera for laparoscopic examination, focusing on the case of minimal instrument-organ contact force rather than manipulating or suturing the organs. Therefore, capping the maximum tip load at around 0.1 N for characterising the soft robot is reasonable. In practice, we conducted experiments with tip loads of 0 g, 4 g, 8 g, and 12 g to assess the soft robot's force capability.

The elongation and bending performances of the soft robot are characterised, with the actuation pressure ranging between 0 bar and 1.6 bar. The bending characterisation experiments
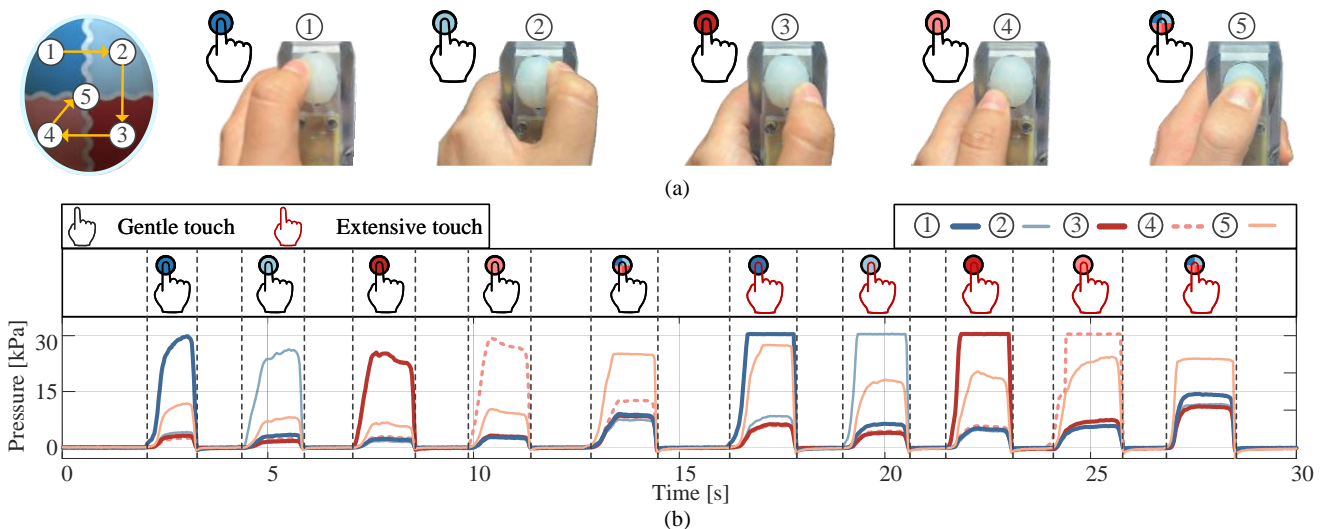


Fig. 5. Touching-sensing capabilities of the multi-cavity soft button. (a) Sequence of touches to the soft button, starting with the dark blue in the top left and proceeding clockwise around the surface to stimulate each cavity on the first layer. The touch sequence finishes by pressing the centre cavity. (b) Relative pressure for each stimulated cavity, touched with the gentle touch and the extensive touch.
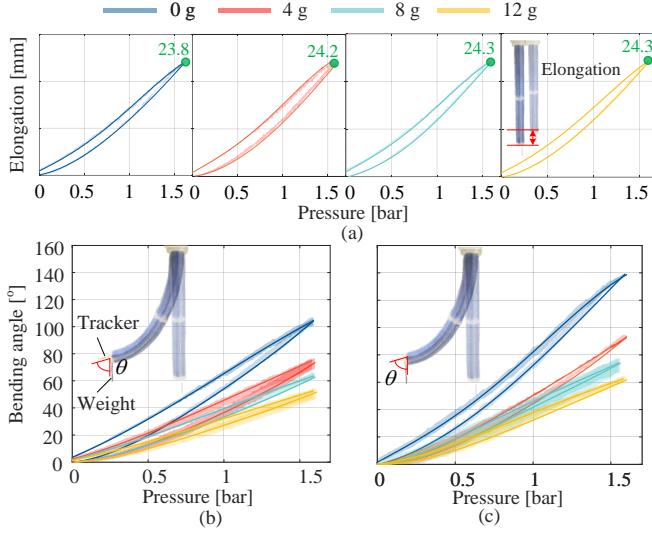
Fig. 6. Characterisation results for the soft robot under varying tip loads of 0 g, 4 g, 8 g, and 12 g. (a) Elongation distances. Bending angles when (b) one chamber pair is actuated and (b) two chamber pairs are actuated in each robot segment.

include tests involving the actuation of one chamber pair and two chamber pairs. An NDI electromagnetic tracker is affixed to the robot tip to record the elongation distances and bending angles at the robot tip. Details of the characterisation setup are reported in [56].

Fig. 6 reports the characterisation results. As illustrated in Fig. 6(a), the maximum elongation distances under various loads are similar, ranging between 23 mm and 25 mm. In contrast, Figs. 6(b)-(c) reveal a significant impact of tip loads on the bending performances. Specifically, when the loads increase from 0 g to 12 g under one chamber pair actuation, the maximum bending angle is $104.3°$, $74.5°$, $63.1°$ and $51.6°$, respectively. In addition, when two chamber pairs are actuated, the bending angle is $138.6°$, $93.5°$, $74.0°$ and $61.6°$ for loads of 0 g, 4 g, 8 g, and 12 g, respectively.

### B. Characterisation of the Touch Interface

The performance of the multi-cavity soft interface is characterised under varying stimuli, considering different touch orientations and intensities. In the characterisation test, the pressure variations ($\Delta P_i$, $i = 1 \cdots 5$) in five cavities are monitored by five pressure sensors (see Fig. 3(c)). As shown in Fig. 5(a), the touch sequence begins with the second cavity on the top left side of the touch interface and proceeds clockwise around the surface. This sequential process stimulates different touch orientations and concludes with a press at the centre. Two tests are conduced, encompassing a gentle and a extensive touch. In the first test sequence, four cavities were pressed gently with a slight compression to the centre cavity (i.e., the 5th cavity), and the indentation depth is limited to smaller than 2 mm. In the second test sequence, the response of the touch interface exhibited to an extensive touch is evaluated, and the centre cavity has a significant pressure variation ($\Delta P_5$).

Fig. 5(b) reports the pressure response of the touch interface during two touch sequences. In the gentle touch sequence, the average peak pressure in the stimulated cavity reaches $27.6\,\text{kPa}$, while the pressure in unstimulated cavities remains below $10\,\text{kPa}$. The average pressure in cavity 5 differs by $12.2\,\text{kPa}$ between gentle and extensive touch modes for gestures 1-4, with gentle touch averaging $10.63\,\text{kPa}$ and extensive touch averaging $22.43\,\text{kPa}$. When the touch interface is compressed from the top, as demonstrated in the fifth gesture of Fig. 5(a), the pressure in all five chambers increases simultaneously, and the centre cavity exhibits the largest pressure, reaching $25.7\,\text{kPa}$. In the second sequence with an extensive touch, the maximum pressure in the stimulated cavities reaches $30.2\,\text{kPa}$. During the extensive touch, the pressure $\Delta P_5$ in the centre cavity increases from $10\,\text{kPa}$ in the gentle touch test to a range of $18.7\,\text{kPa}$ to $27.8\,\text{kPa}$. In both gentle and extensive touch tests, while gesture 5 (see Fig. 5(a)) results in similar pressure responses, where the pressure in the centre cavity surpasses that in the other four cavities, reaching up to $25.2\,\text{kPa}$. The time to reach maximum pressure differs, with 0.52 s for the extensive touch and 0.27 s for the gentle touch. The similar peak pressure values in both touch modes may be attributed to the larger volume of cavity 5 compared to the other cavities. Specifically, the volume is $314.2\,\text{mm}^3$ and $144.0\,\text{mm}^3$ for the central cavity and the four directional cavities, respectively. A larger volume of sealed air results in smaller pressure variations and reduced sensitivity to touch intensity. Please note that the measured pressure saturates at about 30 kPa in the extensive touch mode, due to the pressure sensor's measurement range.

## IV. SYSTEM MODELLING AND CONTROL STRATEGY

### A. Kinematics of the Soft Robot

As illustrated in Fig. 2, the soft robot has a slender and continuum structure, with variable curvatures subjected to actuation. Our previous work reports the robot kinematics based on the static Cosserat rod model [4], considering the nonlinear strain-stress relation of soft materials. In summary, the robot configuration, including the displacement vector $p(s)$ and the rotation matrix $R(s)$, is described via differentiation with respect to the curve length $s$ along the central line of the robot, which yields

$$p_{,s}(s) = R(s)v(s), \quad R_{,s}(s) = R(s)\hat{u}(s), \tag{1}$$

where $(\cdot)_{,s}$ denotes the differentiation regard to $s$. $v(s)$ and $u(s)$ are the local strain vectors and bending curvatures. $(\hat{\cdot})$ is the mapping from $\mathbb{R}^3$ to $\mathfrak{so}(3)$ [57]. Derivatives of the internal force $n(s)$ and moment $m(s)$ along the arc $s$ are

$$\begin{aligned} n_{,s}(s) &= -f_e(s) + f_P(s), \\ m_{,s}(s) &= -\hat{p}_{,s}(s)n(s) - l_e(s) + l_P(s). \end{aligned} \tag{2}$$

$f_e(s)$ and $l_e(s)$ are the distributed external force and moment. $f_P(s)$ and $l_P(s)$ are the distributed force and moment resulting from pressurised chambers, which can be obtained from [4]. For a two-segment robot with a rigid connection part, [4] also reports required intermediate boundary conditions, including kinematic continuity and force/moment balances.

Equations (1) and (2) can be integrated using the Fourth-order Runge-Kutta method and solved by shooting methods.

TABLE I
SUMMARY OF VARIABLES

| Symbol | Description |
|---|---|
| $\Delta P$ | $\in \mathbb{R}^5$, pressure variation in the touch interface |
| $(\hat{\cdot})$ | Mapping from $\mathbb{R}^3$ to $\mathfrak{so}(3)$ |
| $(\cdot)^-, (\cdot)^+$ | Left or right limits of a variable along the robot's central line |
| $(\cdot)_{,s}$ | $\partial(\cdot)/\partial s$, derivation of a variable with the arc length $s$ |
| $R(s)$ | Rotation matrix along the robot |
| $p(s)$ | Translation vector along the robot. |
| $v(s)$ | Local strain vector |
| $u(s)$ | Local bending curvature vector |
| $n(s)$ | Internal force along the robot |
| $m(s)$ | Internal moment along the robot |
| $f_e(s)$ | Distributed external force vector per unit $s$ |
| $l_e(s)$ | Distributed external moment vector per unit $s$ |
| $f_P(s)$ | Distributed force vector from pressurisation per unit $s$ |
| $l_P(s)$ | Distributed moment vector from pressurisation per unit $s$ |
| $F_P(t)$ | Tip actuation force vector, expressed in the global frame |
| $m_P(t)$ | Tip actuation moment vector, expressed in the global frame |
| $F_e(t)$ | External tip force vector, expressed in the global frame |
| $m_e(t)$ | External tip moment vector, expressed in the global frame |
| $\phi_d$ | Calculated touch orientation |
| $P_{nom}$ | Calculated touch intensity |
| $\phi_i$ | Position angle of the $i$th touch interface's cavity |
| $c_i$ | Touch vector of the $i$th touch interface's cavity |
| $P_{i,0}$ | Initial cavity pressure without touch |
| $\delta_P$ | Threshold value for determining variations in cavity pressure |
| $\theta_r$ | Tip bending angle of the soft robot |
| $\phi_r$ | Angle of the bending plane of the soft robot |
| $b_r$ | Summed chamber vector of the soft robot |
| $b_i$ | The $i$th chamber vector of the soft robot |
| $B_i$ | Amplitude of the $i$th chamber vector of the soft robot |
| $\alpha_i$ | Angle between the $i$th chamber pairs and the $x$-axis |
| $P_{ri}$ | Actuation pressure of the soft robot |
| $k_{p\theta}$ | Relationship between the angle $\theta$ and the touch intensity $p_{nom}$ |
| $h$ | Adjustable unitless factor to vary $k_{p\theta}$ |



(a)    (b)

(c)

Fig. 7. Illustration of the mapping from the (a) user space to the (b) robot space. (c) Schematic of operation principles.

To this end, boundary conditions at the robot tip need to be satisfied, yielding

$$n(t^-) = F_P(t^-) + F_e(t^+), \; m(t^-) = m_P(t^-) + m_e(t^+). \quad (3)$$

The superscripts $^-$ and $^+$ denote the left and right limits. $F_e(t^+)$ and $m_e(t^+)$ are the external applied tip force and moment. $F_P(t^-)$ and $m_P(t^-)$ are the total pressurisation force and moment at the manipulator's tip expressed in the global frame. Details of the numerical implementation of the kinematics model are in [4], [57]. In this work, please note that the kinematics model is exclusively for the purpose of visualising robot at different actuation pressure during the operation.

### B. Control Strategy and Operation Principles

To operate the soft robot using the touch interface reported in Section II-B, this section proposes the corresponding control strategy as summarised in Fig. 7. The control strategy maps the touch information to the motions of the soft robot.

*1) Mapping between the User and Robot Space:* In the user space, the cavity pressure variation $\Delta P \in \mathbb{R}^5$ in the touch interface reflects the touch information. Here, $\phi_d \in (0°, 360°)$ and $P_{nom}$ are defined to describe the touch orientation and intensity. To describe the touch on the four cavities in the first layer, the touch vector $c_i$ $(i = 1 \cdots 4)$ is defined as

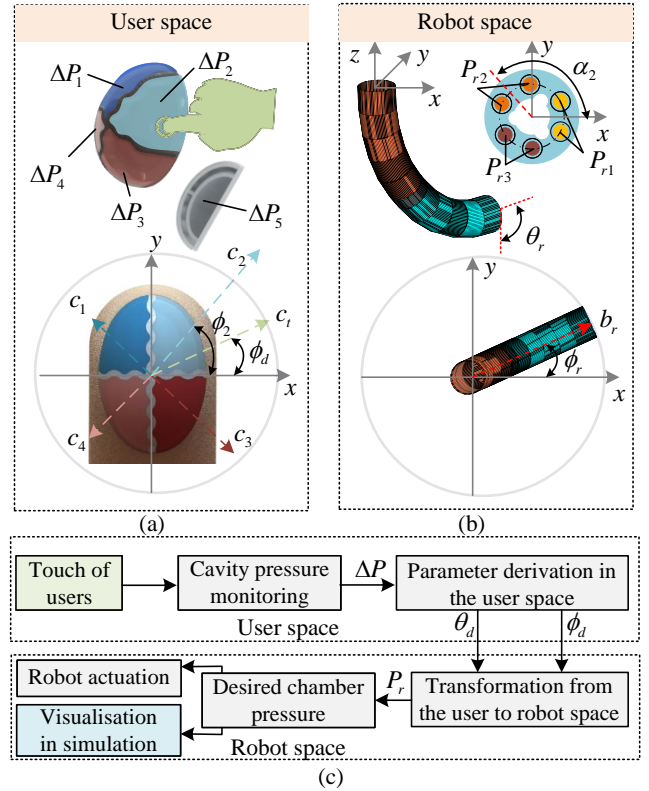$$c_i = \Delta P_i[\cos\phi_i, \; \sin\phi_i], \; \phi_i = \frac{(5-2i)\pi}{4}, \quad (4)$$

where $\phi_i$ denotes the position angle of the $i$th cavity, as shown in Fig. 7(a). The calculation of $\Delta P_i$ needs to consider the influence from pressure variation of other cavities, as illustrated in Fig. 5(b). To this end, $\Delta P_i$ is calculated by

$$\begin{cases} \Delta P_i = 0, & \text{if } P_i - P_{i,0} < \delta_P, \\ \Delta P_i = P_i - P_{i,0}, & \text{if } P_i - P_{i,0} > \delta_P, \end{cases} \quad (5)$$

where $P_{i,0}$ is the initial cavity pressure without touch, and $\delta_P$ is a threshed value to mitigate the interference of other cavities. Sum of the touch vector $c_t$ determines $\phi_d$ and $P_{nom}$ and is calculated by

$$c_t = \sum_{i=1}^4 c_i, \; \phi_d = \operatorname{atan2}(c_t(2), c_t(1)), \; P_{nom} = ||c_t||_2, \quad (6)$$
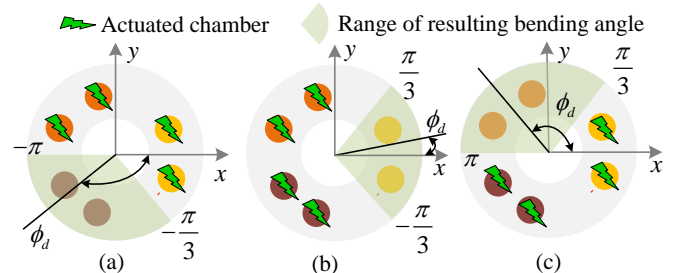


Fig. 8. Illustration of resulting ranges of bending angles when (a) the first and second, (b) the second and third, and (c) the first and third chamber pairs are actuated.

where $P_{nom}$ is the amplitude of $c_t$. $c_t(1)$ and $c_t(2)$ are the first and second component of $c_t$, respectively.

In the robot space, $\theta_r$ and $\phi_r$ denotes the tip bending angle and the out-of-plane angle of the soft robot in the Cartesian space, and $P_{ri}$ is the actuation pressure of the soft robot. (see Fig. 7(b)). To achieve an intuitive control, $\phi_d$ is used directly as the desired angle of $\phi_r$. As such, the touch orientation is mapped to the out-of-plane angle of the soft robot with a ratio of 1:1. In addition, the touch intensity $P_{nom}$ controls the desired bending angle (i.e., $\theta_d$) of the soft robot. A factor $k_{p\theta}$ can be defined as follows

$$\theta_d = k_{p\theta} P_{nom}, \quad (7)$$

where $k_{p\theta}$ has a unit of deg/kPa. $k_{p\theta}$ is the slope of a linear fitting relating the touch intensity $P_{nom}$ with the resulting bending angle of the robot. In fact, $k_{p\theta}$ represents the control sensitivity from the touch interface. The higher the gain, the higher the control sensitivity. In practice, $k_{p\theta}$ needs to be identified from experiments, and Section IV-B2 details the control algorithm to vary $k_{p\theta}$.

*2) Direct Control of the Soft Robot:* As elaborated in Section IV-B1, the desired control variables from the touch interface are $\theta_d$ and $\phi_d$. As illustrated in Fig. 7(b), the summed chamber vector $b_r$ can be defined as

$$b_r = \sum_{i=1}^{3} b_i = \sum_{i=1}^{3} B_i[\cos\alpha_i, \sin\alpha_i], \quad \alpha_i = \frac{2\pi}{3}(i-1), \quad (8)$$

where $b_r$ is a unit vector. $B_i$ $(i=1,2,3)$ is the amplitude of each chamber vector. $b_i$ denotes the $i$th chamber vector. $\alpha_i$ is the angle between the $i$th chamber pairs and the $x$-axis.

Fig. 8 describes range of bending angles when any two adjacent chamber pairs are actuated. For instance, Fig. 8(a) shows that the bending angle is in $[-\pi, -\frac{\pi}{3}]$, when the first
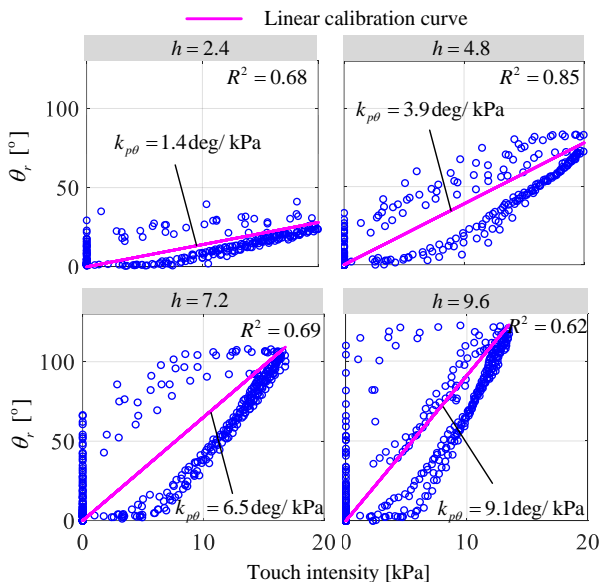


Fig. 9. Results for Experiment 1: Linear calibration curves with four identified $k_{p\theta}$ from experiments when setting four different values of $h$.

and second chamber pairs are actuated. Considering $\phi_r = \phi_d$ in Fig. 8(a), (9) yields

$$\phi_r = \operatorname{atan} 2(-b_r(2), -b_r(1)), \quad B_3 = 0, \phi_d \in [-\pi, -\frac{\pi}{3}). \quad (9)$$

Equation (9) can be rewritten as

$$B_1 \cos 0 + B_2 \cos\left(\frac{2}{3}\pi\right) = -\cos\theta_d,$$
$$B_1 \sin 0 + B_2 \sin\left(\frac{2}{3}\pi\right) = -\sin\theta_d. \quad (10)$$

Reformulating (10) in a matrix form yields

$$\begin{bmatrix} B_1 \\ B_2 \end{bmatrix} = -\begin{bmatrix} \cos 0 & \cos(\frac{2}{3}\pi) \\ \sin 0 & \sin(\frac{2}{3}\pi) \end{bmatrix}^{-1} \begin{bmatrix} \cos\phi_d \\ \sin\phi_d \end{bmatrix}. \quad (11)$$

Solving (11) results in the value of $B_1$ and $B_2$ when $\phi_d \in [-\pi, -\frac{\pi}{3})$.

The actuation pressure $P_{ri}$ (see Fig. 7(b)) is then calculated by $P_{ri} = hP_{nom}B_i$. $h$ is an adjustable unitless factor. Similarly, $P_{ri}$ can be obtained when $\phi_d \in [-\frac{\pi}{3}, \frac{\pi}{3})$ (see Fig. 8(b)) and $\phi_d \in [\frac{\pi}{3}, \pi)$ (see Fig. 8(c)). In summary, the control law for the inverse kinematics control is designed as:

When $\phi_d \in [-\pi, -\frac{\pi}{3})$ :

$$\begin{bmatrix} P_{r1} \\ P_{r2} \end{bmatrix} = -hP_{nom}\begin{bmatrix} \cos 0 & \cos(\frac{2}{3}\pi) \\ \sin 0 & \sin(\frac{2}{3}\pi) \end{bmatrix}^{-1} \begin{bmatrix} \cos\phi_d \\ \sin\phi_d \end{bmatrix},$$

when $\phi_d \in [-\frac{\pi}{3}, \frac{\pi}{3})$ :

$$\begin{bmatrix} P_{r2} \\ P_{r3} \end{bmatrix} = -hP_{nom}\begin{bmatrix} \cos(\frac{2}{3}\pi) & \cos(-\frac{2}{3}\pi) \\ \sin(\frac{2}{3}\pi) & \sin(-\frac{2}{3}\pi) \end{bmatrix}^{-1} \begin{bmatrix} \cos\phi_d \\ \sin\phi_d \end{bmatrix},$$

when $\phi_d \in [\frac{\pi}{3}, \pi)$ :

$$\begin{bmatrix} P_{r1} \\ P_{r3} \end{bmatrix} = -hP_{nom}\begin{bmatrix} \cos(-\frac{2}{3}\pi) & \cos(0) \\ \sin(-\frac{2}{3}\pi) & \sin(0) \end{bmatrix}^{-1} \begin{bmatrix} \cos\phi_d \\ \sin\phi_d \end{bmatrix}, \quad (12)$$

and,

$$P_{r3} = 0, \ \phi_d \in [-\pi, -\frac{\pi}{3}), \ P_{r1} = 0, \ \phi_d \in [-\frac{\pi}{3}, \frac{\pi}{3}),$$
$$P_{r2} = 0, \ \phi_d \in [\frac{\pi}{3}, \pi). \quad (13)$$

Equations (12) and (13) offer the direct mapping between the user space and the robot space. $\phi_d$ and $\phi_r$ have a ratio of 1:1, which enable an intuitive control when users press the touch interface. For the bending angle control, the gain factor $h$ essentially regulates the control sensitivity $k_{p\theta}$ from the touch interface.

## V. EXPERIMENTAL EVALUATION

This section assesses the control strategy proposed in IV-B and evaluates the design of the developed soft robotic laparoscopy device with an integrated touch interface. Specifically, Experiment 1 validates the control strategy on a test bench, while Experiment 2 evaluates the usability of the medical device by participants in a phantom environment.
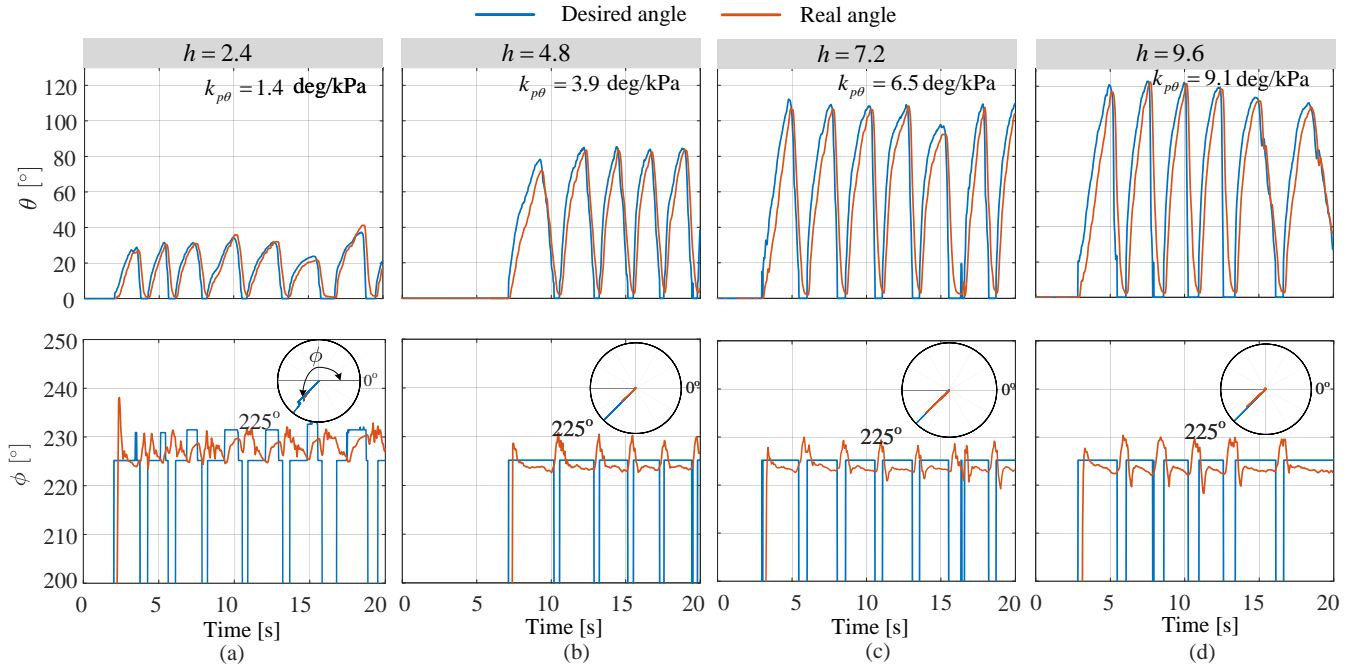
Fig. 10. Results for Experiment 1: Comparison between desired and real bending angles $\theta$ and out-of-plane angles $\phi$, when only one cavity is pressed. The obtained results when the gain factor (a) $h = 2.4$, (b) $h = 4.8$, (c) $h = 7.2$, and (d) $h = 9.6$. $k_{p\theta}$ is identified in Fig. 9.
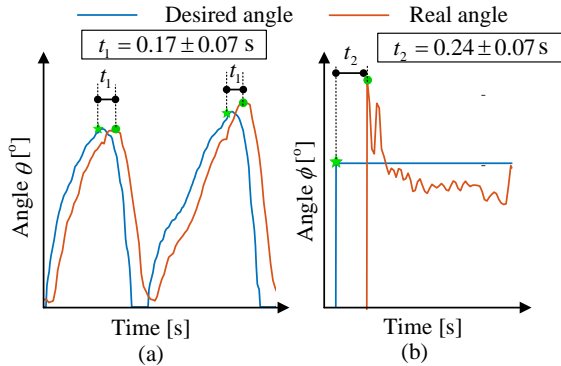


Fig. 11. Results for Experiment 1: Time delay analysis of (a) the bending angle $\theta$ and (b) the out-of-plane angle $\phi$. The time delay is defined as the difference in time between the peaks of the desired angle (green star) and the actual angle (green circle), denoted by $t_1$ and $t_2$.

## A. Experiment 1 - Control Assessment of the Touch Interface

*1) Experimental Protocol:* To validate the control strategy proposed in Section IV-B, the two-segment robot was operated via the touch interface. The robot was amounted upside down onto a test rig [56]. One electromagnetic sensor was attached at the tip of the robot to record the bending angle $\theta_r$ and the out-of-plane angle $\phi_r$ during the operation. Two sets of experiments were conducted:

- The third cavity was randomly pressed with different touch intensities over 5~7 times in 20 seconds. Four gain factors $h$ of 2.4, 4.8, 7.2 and 9.6 were chosen.
- The touch interface was randomly pressed with varying touch intensities and orientation in 120 seconds. The gain factor $h$ is chosen as 7.2. The touch frequency was applied from a lower ($0.2 \sim 1$ Hz) to a higher range (1

$\sim 4$ Hz).

All the data were collected and processed using Matlab. The frequency of the data collection was set as 20 Hz.

*2) Results for Experiment 1:* Fig. 9 reports results when only the third cavity is pressed. Regarding the bending angle, the identified $k_{p\theta}$ increases with the gain factor $h$. Specifically, $k_{p\theta}$ values are 1.4, 3.9, 6.5 and 8.6 deg/kPa for $h$ values of 2.4, 4.8, 7.2 and 9.6, respectively. The $R^2$ values of linear curves range between 0.62 and 0.85. Furthermore, Fig. 10 reports that the desired out-of-plane angle $\phi_d$ from the touch interface remains consistently close to a constant value in all tests when only the third cavity is pressed. Specifically, $\phi_d$ remains stable at $225°$ when $h = 4.8, 7.2,$ and $9.6$. $\phi_d$ ranges between $225°$ and $235°$ when $h = 2.4$. Table II summaries the steady-state errors between $\phi_d$ and $\phi_r$. The results illustrate that the mean and standard deviation errors are less than $3.0°$ and $2.5°$ when the desired angle is $225°$. Fig. 11 further reports the time delay when controlling the bending and out-of-plane angle. As indicated in Fig. 11, the time delay is defined as the difference in time between the peaks of the desired angle and the real angle. Specifically, the mean time delay for the bending angle is 0.17 seconds, and for the out-of-plane angle, it is 0.24 seconds. The standard deviation of the time delay for both angles is similar, at 0.07 seconds.

Fig. 12 reports the experimental results with varying touch orientation and intensity. Specifically, Fig. 12(a) demonstrates that the touch orientation spans from $0°$ to $360°$, and the maximum value of $P_{nom}$ reaches 25.5 kPa. Figs. 12(c)-(d) demonstrate that $\theta_r$ and $\phi_r$ are controlled to follow the desired angles. Moreover, the results illustrate that the control accuracy is impacted by the touch frequency. In the first 100 seconds, touch is applied at a low frequency of around $0.2 \sim 1$ Hz.
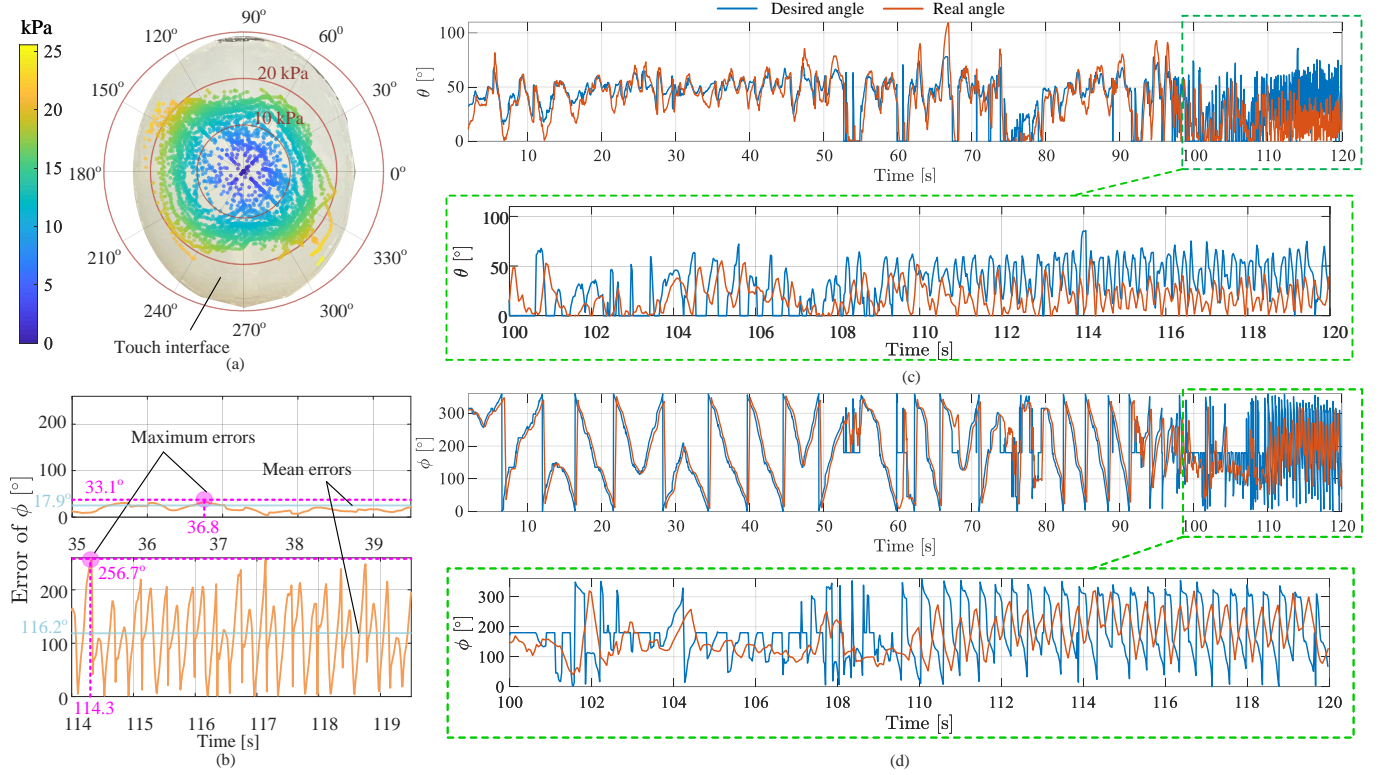
Fig. 12. Results for Experiment 1: Comparison of desired and real $\theta$ and $\phi$ under (a) varying touch orientation and intensity. (b) Errors of $\phi$ when time is between 35∼40 seconds and $114 \sim 120$ seconds. Comparisons between (c) $\theta$ and (d) $\phi$. Here, $\theta_d \in 0° \sim 110°$ and $\phi_d \in 0° \sim 360°$.

The frequency then increases to 1∼ 4 Hz during $100 \sim 120$ seconds. In general, a better control accuracy is observed when the touch frequency is less than 1 Hz. For instance, Fig. 12(b) indicates that the maximum and mean errors of $\phi$ are 33.1° and 17.9° respectively, during 35∼40 seconds. In contrast, these errors increase to 256.7° and 116.2° during $114 \sim 120$ seconds. As demonstrated in Figs. 12(c)-(d), the amplitudes of $\theta_r$ and $\phi_r$ are only about 50% ∼ 80% of desire values during $100 \sim 120$ seconds. Supplementary Video demonstrates the operation of the device using various touch frequencies on the test rig.

### B. Experiment 2 - Usability Test

*1) Experimental Protocol:* Five points on the surface of a colon were marked from 1 to 5, and the colon was placed inside a human phantom as shown in Fig. 13. Participants were asked to operate the laparoscopy device to find these five points and identify their positions, guided by the camera view and the visualised soft robot. Specifically, the simulated

robot (see Section IV-A) was displayed in real time, providing information on the robot state subjected to touch input. Before the actual test, participants were required to conduct a hands-on training session for 3 minutes, to familiarise themselves with the operation of the laparoscopy and its intuitive control. The time taken for each participant to complete the task was recorded. Additionally, all participants were required to answer two questions after the trial. The questions are:

- The usefulness of the simulated robot: "Not useful (1)", "Slightly useful (2)", "Useful (3)", "Fairly useful (4)", "Very useful (5)".
- The difficulty of the device operation: "Not easy (1)", "Slightly easy (2)", "Easy (3)", "Fairly easy (4)", "Very easy (5)".

In total, there were 9 male and 2 female non-expert participants, within the age ranging from 23 to 35 years old. The study received ethical approval from the UCL Research Ethics Committee (application number 12453/001).

*2) Results for Experiment 2:* Fig. 14 reports the results of the usability test. Fig. 14(a) indicates the testing time for 11 trials, with the average time being 127.55 s. The maximum testing time recorded is 211 s, and the minimum is 38 s. Fig. 14(b) shows the assessment results of the device control, where the overall average score is 3.91, close to the category of "Fairly easy". Additionally, the scores from all participants are above 3, i.e., falling into the scope of "Easy". Fig. 14(c) demonstrates that the average score for the usefulness of the simulated robot is 2.09 (i.e., "Slightly useful"), with four

TABLE II
SUMMARY OF STEADY-STATE ERRORS OF $\phi$ USING FOUR GAIN FACTORS

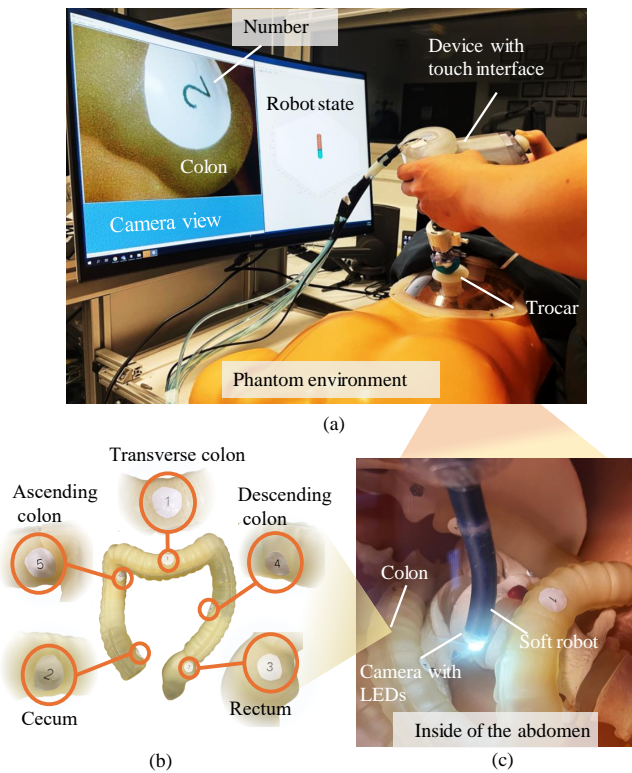| Gain factor | Mean error [°] | Standard deviation [°] |
|---|---|---|
| 2.4 | 2.81 | 2.15 |
| 4.8 | 1.65 | 0.85 |
| 7.2 | 2.11 | 1.37 |
| 9.6 | 2.27 | 1.51 |

Fig. 13. (a) Demonstration of the experimental setup for the usability test in a phantom environment. (b) Illustration of the position of five markers on a printed colon model. (c) Abdominal view. Supplementary Video demonstrates operating the developed handheld laparoscopy device in the phantom.

participants reporting that the simulated robot is not useful, giving a score of 1.

Fig. 15 reports the accuracy of identifying five marker positions on the colon in a confusion matrix. The diagonal of the matrix indicates that the success rates are 100%, 72.7%, 90.9%, 63.6%, and 81.8% for markers 1 to 5, respectively. Generally, markers 2 and 4 exhibit lower success rates. The average success rate across the five positions is 81.8%. Moreover, for the simulated robot (see Fig. 13(a)), it is noteworthy that kinematics modelling errors are less than 5% of the original robot length [4] by conducting parameter identification.

## VI. DISCUSSIONS OF RESULTS

Experiment 1 validates the operation effectiveness of the proposed control strategy (refer to Section IV-B) for the developed soft laparoscopy device. Both the bending angle $\theta_r$ and the out-of-plane angle $\phi_r$ in the robot space are controlled via the touch interface. Notably, the ratio $\phi_r/\phi_d = 1$ allows for intuitive control of the robot when the user presses the touch interface. In contrast, the bending angle $\theta_r$ is proportionally controlled relative to the touch intensity, with adjustable gain factors $k_{p\theta}$. It is essential to highlight that our bending angle controller focuses on correlating the touch intensity to the resulting bending angle rather than controlling the absolute value of $\theta_r$. In addition, Fig. 10 illustrates that the controlled out-of-plane angle $\phi_r$ doesn't return back to zero, which is attributed to the hysteresis of the silicone material. In the experiment,

it is observed that the displacements along the x- and y-axis don't go back to zero when the soft robot transitions from an actuated state to an unactuated state, each exhibiting an offset of approximately 1 mm. In this case, the calculated remains close to the desired value of 225 degrees. Fig. 12 indicates that the system has a bandwidth frequency of around 1 Hz, since the achieved amplitudes of $\theta_r$ and $\phi_r$ are approximately 50% $\sim$ 80% of desire values when the touch frequency exceeds 1 Hz. The robot control (see Section IV-B2) is achieved by mapping the touch information to the robot motion directly, ensuring high computational efficiency compared to solving inverse kinematics problems [4].

Experiment 2 conducts the usability test, scoring 3.91/5 (i.e., fairly easy), indicating that a satisfying operation of the developed device is achieved. In addition, it is also reported that the visualisation of the simulated robot only demonstrates slight usefulness, scoring 2.09/5. This suggests that participants primarily rely on the camera view during the operation. Moreover, a large variation in the time spent is observed, ranging from 38 s to 211 s. This can be attributed to the movements of the device through the trocar port (i.e., the pivot point). Generally, it takes less time when participants utilise movements around the pivot point. This might result from the fact that the simulated robot only provides the motions of the soft robot, while lacking information on the entire phantom environment. Hence, when the soft robot was trapped in obstacles, the user needed extra time to realise it and extricate the robot from these obstacles, a situation that occurred in trials 4 and 5. Notably, the forward kinematics model, as reported in Section IV-A, is exclusively for assessing the usefulness of offering auxiliary visualisation of the soft robot in a simulation environment during the operation (see the Supplementary Video).

Fig. 15 illustrates that markers 1, 3, and 5 have a higher accuracy rate, which could be attributed to the colon structure (see Fig. 13(b)). For instance, marker 3, being close to the rectum area with a distinguished structure from other parts of the colon, facilitated easier identification. Markers 2 and 4, located at the inside bottom, were more difficult to approach, resulting in lower accuracy during the test. Notably, all participants are non-experts with minimal knowledge of colon structure, which might influence the success rate reported in Fig. 15. Involving clinicians to evaluate the performance of the developed device will be an important aspect to explore in future studies.

In comparison to existing soft robots featuring reinforced chambers [27], [28], [58], [59], where the soft robot has a diameter over 12 mm, our soft instrument has the smallest diameter of 11.5 mm. This miniaturised dimension allows our soft robotic device to seamlessly fit to the commonly available 12 mm trocar port [22]. In addition, our medical device is compact, as the touch control interface is integrated to the assembly of our developed medical device (see Fig. 4). In contrast, to operate soft robotic devices, additional auxiliary devices or mechanisms, e.g., continuum user interfaces [38], [41] and joysticks [24], [35], are usually required in existing work. Notably, the touch interface is low-cost, as it is exclusively made of silicone structure sealed with air. The
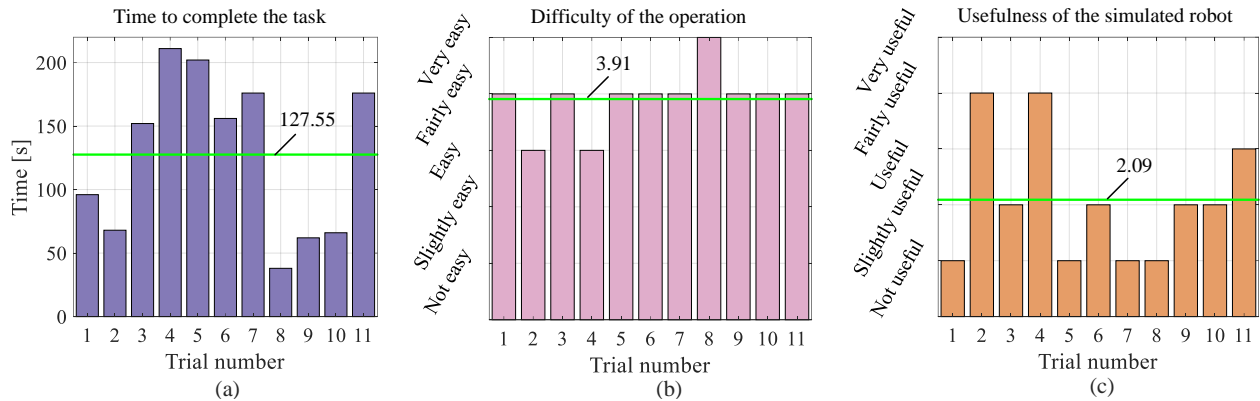
Fig. 14. Results for Experiment 2: Usability test results of eleven participants. (a) Time to complete the task. (b) Assessment of the device operation. (c) Usefulness evaluation of visualising the simulated robot during the operation. Green lines denote the averaged values.

components listed in Table VI cost approximately £ 252.20, with the silicone used for the touch interface accounting for less than 1% of this overall cost.

Studies illustrate that the response time of pneumatic-driven soft medical devices ranges from 0.05 to 1 second [60], indicating these systems exhibit a low bandwidth. Similarly, our system has an average response time of 0.17 to 0.24 seconds (Fig. 11). This primarily explains why our system achieves satisfactory accuracy at frequencies around 1 Hz and below, as shown in Fig. 12. Our achieved working frequency is also comparable with other soft robotic devices. For instance, the bandwidth of a fluid-driven soft robotic laser ablation device was reported to be 1 Hz in [61]. The response time of pneumatic-driven soft robots depends on various factors, including the bandwidth of the pressure control devices, the size of air tubes and actuation chambers, and the inherent properties of compliant materials, such as hysteresis. For instance, our system's pressure control has a time constant of about 0.085 seconds identified in [56]. Potential approaches to improve system bandwidth include reducing the length and diameter of air pipes, deploying high-performance pressure control devices, or exploring alternative soft materials.

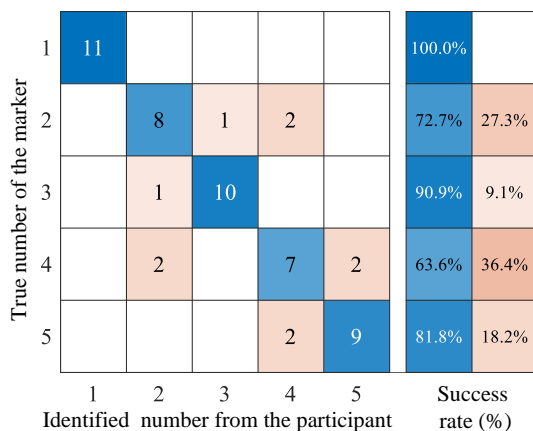In this work, our contribution is to innovate the touch

### TABLE III
### HARDWARE COST OF THE HANDHELD LAPAROSCOPIC DEVICE

| Component | Approximate cost [£] |
|---|---|
| Silicone (Ecoflex 10, Dragon Skin 10 and 20) | 4 |
| Tip-mounted camera | 20 |
| Reinforcement fibre | 0.2 |
| Arduino Due | 29 |
| Pressure sensors | 75 |
| Connectors and cables | 15 |
| PCB manufacturing | 10 |
| 3D printing | 100 |
| Total price | 252.2 |

control interface of soft robotic devices, and we successfully demonstrate applying the developed soft instrument for laparoscopic examination with lower instrument-organ contact force of 0.1 N. However, tasks such as manipulating or suturing organs require forces of several Newtons [55]. To meet this challenge, it is essential to enhance the payload capability of soft robots. First, stiffer material can be investigated to improve payload capability of soft robots without changing the robot dimension. For example, study in [62] reports the tip force of a fibre-reinforced soft actuator increases with the stiffness of the soft material. Specifically, force ranges are 2-3 N, 5-8 N and 9-15 N for soft robots made of EcoFlex 30, Dragon Skin 10 and Dragon Skin 20, respectively. Exploring stiffer silicone materials, such as Dragon Skin 20, could be a promising direction for future work. Second, embedding stiffening structures [63], such as layers, granular jamming mechanisms, or stiffening tendons, can also enhance robot payload. Although these structures may occupy additional space, recent advancements have allowed us to miniaturize soft robots to diameters smaller than 10 mm [64]. This miniaturization opens up the possibility of integrating stiffening structures, thereby achieving higher payload capacities while ensuring compatibility with the 12 mm trocar.

## VII. CONCLUSIONS

This paper has presented the design and evaluation of a flexible handheld soft robotic laparoscopy device featuring an integrated multi-cavity control interface. The touch interface



Fig. 15. Results for Experiment 2: Confusion matrix chart for identifying positions of five markers on the colon.

offers an intuitive control solution for the soft robot during surgical procedures. The feasibility of the device and the efficacy of the control strategy were validated through experiments. In this work, the two-segment robot was controlled in the same manner. Future work will involve controlling the two segments independently to achieve more dexterous navigation. Subsequent efforts will include evaluating the developed laparoscopy device in collaboration with clinicians, potentially conducting experiments in more realistic scenarios alongside other medical instruments. Furthermore, investigating the incorporation of haptic feedback into the touch interface is worthwhile. This enhancement aims to provide information about the interaction between the robotic instrument and its environment, thereby further enhancing the intuitive control of the device.

## Acknowledgement

## References

[1] G.-Z. Yang *et al.*, "Medical robotics—regulatory, ethical, and legal considerations for increasing levels of autonomy," *Sci. Robot.*, vol. 2, no. 4, p. eaam8638, 2017.

[2] M. Yip *et al.*, "Artificial intelligence meets medical robotics," *Science*, vol. 381, no. 6654, pp. 141–146, 2023.

[3] A. Alian *et al.*, "Current engineering developments for robotic systems in flexible endoscopy," *Tech. Innov. Gastrointest. Endosc.*, vol. 25, no. 1, pp. 67–81, 2023.

[4] J. Shi, S. Abad Guaman, J. Dai, and H. Wurdemann, "Position and orientation control for hyperelastic multisegment continuum robots," *IEEE/ASME Trans. Mechatronics*, vol. 29, no. 2, pp. 995–1006, 2024.

[5] K.-W. Kwok, H. Wurdemann, A. Arezzo, A. Menciassi, and K. Althoefer, "Soft robot-assisted minimally invasive surgery and interventions: Advances and outlook," *Proc. IEEE*, vol. 110, no. 7, pp. 871–892, 2022.

[6] J. Burgner-Kahrs, D. C. Rucker, and H. Choset, "Continuum robots for medical applications: A survey," *IEEE Trans. Robot.*, vol. 31, no. 6, pp. 1261–1280, 2015.

[7] D. Wu *et al.*, "Development of a novel ball-and-socket flexible manipulator for minimally invasive flexible surgery," *IEEE Trans. Med. Robot. Bionics.*, vol. 5, no. 2, pp. 278–288, 2023.

[8] G.-B. Bian *et al.*, "Design and nonlinear error compensation of a multisegment soft continuum robot for pulmonary intervention," *IEEE Trans. Med. Robot. Bionics.*, vol. 5, no. 4, pp. 832–842, 2023.

[9] M. Cianchetti, C. Laschi, A. Menciassi, and P. Dario, "Biomedical applications of soft robotics," *Nat. Rev. Mater.*, vol. 3, no. 6, pp. 143–153, 2018.

[10] Y. Wang and Q. Xu, "Design of a new wrist rehabilitation robot based on soft fluidic muscle," in *IEEE/ASME Int. Conf. Adv. Intell. Mechatron*, 2019, pp. 595–600.

[11] A. Stilli *et al.*, "Airexglove—a novel pneumatic exoskeleton glove for adaptive hand rehabilitation in post-stroke patients," in *Proc. IEEE Int. Conf. Soft Robot.*, 2018, pp. 579–584.

[12] G. Shi *et al.*, "Fluidic haptic interface for mechano-tactile feedback," *IEEE Trans. Haptic*, vol. 13, no. 1, pp. 204–210, 2020.

[13] G. Shi, A. Shariati, I. Eames, and H. Wurdemann, "Modelling the compression of a soft ellipsoid fingertip," *Soft Matter*, vol. 18, no. 47, pp. 9076–9085, 2022.

[14] H. A. Sonar, J.-L. Huang, and J. Paik, "Soft touch using soft pneumatic actuator–skin as a wearable haptic feedback device," *Adv. Intell. Syst.*, vol. 3, no. 3, p. 2000168, 2021.

[15] T. Amadeo *et al.*, "Soft robotic deployable origami actuators for neurosurgical brain retraction," *Front. Rob. AI*, vol. 8, p. 731010, 2022.

[16] M. McCandless *et al.*, "A soft robot for peripheral lung cancer diagnosis and therapy," *Soft Rob.*, vol. 9, no. 4, pp. 754–766, 2022.

[17] J. Zhang *et al.*, "Soft hybrid actuated hierarchical bronchoscope robot for deep lung examination," *IEEE Rob. Autom. Lett.*, vol. 9, no. 1, pp. 811–818, 2024.

[18] E. T. Roche *et al.*, "Soft robotic sleeve supports heart function," *Sci. Transl. Med.*, vol. 9, no. 373, p. eaaf3925, 2017.

[19] J. Rogatinsky *et al.*, "A multifunctional soft robot for cardiac interventions," *Sci. Adv.*, vol. 9, no. 43, p. eadi5559, 2023.

[20] T. Gopesh *et al.*, "Soft robotic steerable microcatheter for the endovascular treatment of cerebral disorders," *Sci. Rob.*, vol. 6, no. 57, p. eabf0601, 2021.

[21] C. Girerd, A. Alvarez, E. W. Hawkes, and T. K. Morimoto, "Material scrunching enables working channels in miniaturized vine-inspired robots," *IEEE Trans. Robot.*, vol. 40, pp. 2166–2180, 2024.

[22] S.-A. Abad, A. Arezzo, S. Homer-Vanniasinkam, and H. A. Wurdemann, "Soft robotic systems for endoscopic interventions," in *Endorobotics*, 2022, pp. 61–93.

[23] N. Garbin *et al.*, "A disposable continuum endoscope using piston-driven parallel bellow actuator," in *Int. Symp. Med. Robot.*, 2018, pp. 1–6.

[24] R. Caprara *et al.*, "A platform for gastric cancer screening in low-and middle-income countries," *IEEE Trans. Biomed. Eng.*, vol. 62, no. 5, pp. 1324–1332, 2014.

[25] A. Arezzo *et al.*, "Total mesorectal excision using a soft and flexible robotic arm: a feasibility study in cadaver models," *Surg. Endosc.*, vol. 31, pp. 264–273, 2017.

[26] S. Treratanakulchai *et al.*, "Development of a 6 DOF soft robotic manipulator with integrated sensing skin," in *Proc. IEEE/RSJ Int. Conf. Intell. Robots Syst.*, 2022, pp. 6944–6951.

[27] J. Shi, W. Gaozhang, and H. A. Wurdemann, "Design and characterisation of cross-sectional geometries for soft robotic manipulators with fibre-reinforced chambers," in *Proc. IEEE Int. Conf. Soft Robot.*, 2022, pp. 125–131.

[28] H. Abidi *et al.*, "Highly dexterous 2-module soft robot for intra-organ navigation in minimally invasive surgery," *Int. J. Med. Robot. Comput. Assist. Surg.*, vol. 14, no. 1, p. e1875, 2018.

[29] C. C. Nguyen *et al.*, "A handheld hydraulic soft robotic device with bidirectional bending end-effector for minimally invasive surgery," *IEEE Trans. Med. Robot. Bionics.*, vol. 5, no. 3, pp. 590–601, 2023.

[30] M. Csencsits, B. Jones, W. McMahan, V. Iyengar, and I. Walker, "User interfaces for continuum robot arms," in *Proc. IEEE/RSJ Int. Conf. Intell. Robots Syst.*, 2005, pp. 3123–3130.

[31] E. Almanzor *et al.*, "Static shape control of soft continuum robots using deep visual inverse kinematic models," *IEEE Trans. Robot.*, vol. 39, no. 4, pp. 2973–2988, 2023.

[32] A. Amaya, D. D. Arachchige, J. Grey, and I. S. Godage, "Evaluation of human-robot teleoperation interfaces for soft robotic manipulators," in *Int. Symp. Robot Hum. Interact. Commun.*, 2021, pp. 412–417.

[33] B. Ouyang, Y. Liu, H.-Y. Tam, and D. Sun, "Design of an interactive control system for a multisection continuum robot," *IEEE/ASME Trans. Mechatronics*, vol. 23, no. 5, pp. 2379–2389, 2018.

[34] J. Shi and H. Wurdemann, "Design and control of a tele-operated soft instrument in minimally invasive surgery," in *Hamlyn Symp. Med. Robot.*, 2023, pp. 31–32.

[35] J. Till *et al.*, "Efficient computation of multiple coupled Cosserat rod models for real-time simulation and control of parallel continuum manipulators," in *Proc. IEEE Int. Conf. Robot. Autom.*, 2015, pp. 5067–5074.

[36] F. Campisano *et al.*, "Teleoperation and contact detection of a waterjet-actuated soft continuum manipulator for low-cost gastroscopy," *IEEE Rob. Autom. Lett.*, vol. 5, no. 4, pp. 6427–6434, 2020.

[37] M. Xie, C. Girerd, and T. K. Morimoto, "A 3D haptic trackball interface for teleoperating continuum robots," in *IEEE RAS/EMBS Int. Conf. Biomed. Robot. Biomechatron.*, 2022, pp. 1–8.

[38] N. Garbin *et al.*, "Dual-continuum design approach for intuitive and low-cost upper gastrointestinal endoscopy," *IEEE Trans. Biomed. Eng.*, vol. 66, no. 7, pp. 1963–1974, 2018.

[39] H.-S. Yoon and B.-J. Yi, "Design of a master device for controlling multi-moduled continuum robots," *Proc. Inst. Mech. Eng., Part C: J. Mech. Eng. Sci.*, vol. 231, no. 10, pp. 1921–1931, 2017.

[40] C. G. Frazelle, A. D. Kapadia, and I. D. Walker, "A haptic continuum interface for the teleoperation of extensible continuum manipulators," *IEEE Rob. Autom. Lett.*, vol. 5, no. 2, pp. 1875–1882, 2020.

[41] H. El-Hussieny *et al.*, "Development and evaluation of an intuitive flexible interface for teleoperating soft growing robots," in *Proc. IEEE/RSJ Int. Conf. Intell. Robots Syst.*, 2018, pp. 4995–5002.

[42] A. Giri, R. Bloom, and T. K. Morimoto, "Hapstick: A soft flexible joystick for stiffness rendering via fiber jamming," *IEEE Rob. Autom. Lett.*, vol. 8, no. 7, pp. 4163–4170, 2023.

[43] F. Stroppa *et al.*, "Human interface for teleoperated object manipulation with a soft growing robot," in *Proc. IEEE Int. Conf. Robot. Autom.*, 2020, pp. 726–732.

[44] Y. Zhang, T. Wang, W. He, and S. Zhu, "Human-powered master controllers for reconfigurable fluidic soft robots," *Soft Rob.*, vol. 10, no. 6, pp. 1126–1136, 2023.

[45] C. Girerd and T. K. Morimoto, "Design and control of a hand-held concentric tube robot for minimally invasive surgery," *IEEE Trans. Robot.*, vol. 37, no. 4, pp. 1022–1038, 2020.

[46] R. Mao, L. Gao, W. Gang, and L. Wen, "Literature review of handheld articulating instruments in minimally invasive surgery," *J. Laparoendosc. Adv. Surg. Tech.*, vol. 34, no. 1, pp. 47–54, 2024.

[47] R. J. Hendrick, C. R. Mitchell, S. D. Herrell, and R. J. Webster III, "Hand-held transendoscopic robotic manipulators: A transurethral laser prostate surgery case study," *Int. J. Rob. Res.*, vol. 34, no. 13, pp. 1559–1572, 2015.

[48] M. Leite *et al.*, "Assessment of laparoscopic skills performance: 2D versus 3D vision and classic instrument versus new hand-held robotic device for laparoscopy," *Surg. Innov.*, vol. 23, no. 1, pp. 52–61, 2016.

[49] P.-L. Yen and T.-H. Ho, "Shared control for a handheld orthopedic surgical robot," *IEEE Rob. Autom. Lett.*, vol. 6, no. 4, pp. 8394–8400, 2021.

[50] F. M. Sánchez-Margallo, J. A. Sánchez-Margallo, and A. Szold, "Hand-held devices for laparoscopic surgery," in *New Horizons in Laparoscopic Surgery*. Rijeka: IntechOpen, 2018, ch. 6.

[51] P. Chaillou *et al.*, "Reduced finite element modelling and closed-loop control of pneumatic-driven soft continuum robots," in *Proc. IEEE Int. Conf. Soft Robot.*, 2023, pp. 1–8.

[52] J. Fraś *et al.*, "New STIFF-FLOP module construction idea for improved actuation and sensing," in *Proc. IEEE Int. Conf. Robot. Autom.*, 2015, pp. 2901–2906.

[53] J. W. Garrett, "The adult human hand: some anthropometric and biomechanical considerations," *Hum. Factors*, vol. 13, no. 2, pp. 117–131, 1971.

[54] G. Shi *et al.*, "Design and characterisation of multi-cavity, fluidic haptic feedback system for mechano-tactile feedback," *IEEE Trans. Haptics*, pp. 1–15, 2024.

[55] G. Picod, A. Jambon, D. Vinatier, and P. Dubois, "What can the operator actually feel when performing a laparoscopy?" *Surg. Endosc.*, vol. 19, pp. 95–100, 2005.

[56] J. Shi *et al.*, "Characterisation and control platform for pneumatically driven soft robots: Design and applications," in *Proc. IEEE Int. Conf. Soft Robot.*, 2023, pp. 1–8.

[57] J. Shi, A. Shariati *et al.*, "Stiffness modelling and analysis of soft fluidic-driven robots using Lie theory," *Int. J. Rob. Res.*, vol. 43, no. 3, pp. 354–384, 2024.

[58] A. Diodato *et al.*, "Soft robotic manipulator for improving dexterity in minimally invasive surgery," *Surg. Innov.*, vol. 25, no. 1, pp. 69–76, 2018.

[59] J. Shi, J. C. Frantz *et al.*, "Screw theory-based stiffness analysis for a fluidic-driven soft robotic manipulator," in *Proc. IEEE Int. Conf. Robot. Autom.*, 2021, pp. 11 938–11 944.

[60] J. Zhu *et al.*, "Intelligent soft surgical robots for next-generation minimally invasive surgery," *Adv. Intell. Syst.*, vol. 3, no. 5, p. 2100011, 2021.

[61] G. Fang *et al.*, "Soft robotic manipulator for intraoperative MRI-guided transoral laser microsurgery," *Sci. Robot.*, vol. 6, no. 57, p. eabg5575, 2021.

[62] Y. Sun, H. Feng, I. R. Manchester, R. C. H. Yeow, and P. Qi, "Static modeling of the fiber-reinforced soft pneumatic actuators including inner compression: Bending in free space, block force, and deflection upon block force," *Soft Rob.*, vol. 9, no. 3, pp. 451–472, 2022.

[63] M. Manti, V. Cacucciolo, and M. Cianchetti, "Stiffening in soft robotics: A review of the state of the art," *IEEE Robot. Autom. Mag.*, vol. 23, no. 3, pp. 93–106, 2016.

[64] J. Shi, S.-A. Abad, A. Menciassi, K. Althoefer, and H. A. Wurdemann, "Miniaturised soft manipulators with reinforced actuation chambers on the sub-centimetre scale," in *Proc. IEEE Int. Conf. Soft Robot.*, 2024, pp. 157–164.